aerospace

Article

The Aerodynamic Performance of a Novel Overlapping Octocopter Considering Horizontal Wind

Yao Lei [1,2,*], Jie Wang [1] and Yazhou Li [1]

[1] School of Mechanical Engineering and Automation, Fuzhou University, Fuzhou 350116, China
[2] Key Laboratory of Fluid Power and Intelligent Electro-Hydraulic Control, Fuzhou University, Fuzhou 350116, China
* Correspondence: yaolei@fzu.edu.cn; Tel.: +86-0591-22866791

Abstract: This paper investigates the aerodynamic performance of an overlapping octocopter with the effect of horizontal wind ranging from 0 to 4 m/s using both low-speed wind tunnel tests and numerical simulations. The hovering efficiency and the potential control strategies of the octocopter under the effect of horizontal wind are also validated using blade element momentum theory. The velocity distribution, rotor pressure and vortex of the downwash flow with the horizontal wind are presented using the Computational Fluid Dynamics (CFD) method. Finally, wind tunnel tests were performed to obtain the thrust and power consumption with the rotor speed ranging from 1500 to 2200 rpm for horizontal winds at 0 m/s, 2.5 m/s and 4 m/s. The results showed that horizontal wind decreased the flight efficiency of the planar octocopter and had little effect on the coaxial octocopter. It is also interesting to note that horizontal wind is beneficial for thrust increments at a higher rotor speed and power decrements at a lower rotor speed for the overlapping octocopter. Specifically, the horizontal wind of 2.5 m/s for a lower rpm is presented with a power decrement with proper aerodynamic interference between the rotor blades. Additionally, the overlapping octocopter obtains a higher hover efficiency at 4 m/s compared to traditional octocopters, which is more suitable for flying in a cross wind with a more compact structure.

Keywords: aerodynamics; hover; horizontal wind; overlapping octocopter; UAV

Citation: Lei, Y.; Wang, J.; Li, Y. The Aerodynamic Performance of a Novel Overlapping Octocopter Considering Horizontal Wind. *Aerospace* **2023**, *10*, 902. https://doi.org/10.3390/aerospace10100902

Academic Editors: Anthony D. Gardner and Christian Breitsamter

Received: 31 July 2023
Revised: 13 October 2023
Accepted: 17 October 2023
Published: 22 October 2023

1. Introduction

Rotary Unmanned Aerial Vehicles (UAVs) have become widely used in the military and civilian industries in recent years [1]. Due to the ability to land vertically and hover, they are considered highly maneuverable [2,3] and are applied for battlefield surveillance, border patrol, and even rescue missions [4,5]. For rotary UAVs, a higher thrust and lower power consumption are the key factors to maintain the flight efficiency required to perform complex tasks. In particular, a compact structure with a limited space is also promoted for some tasks, which means that the rotors are closely distributed [6]. In this case, a novel overlapping UAV is designed to fly in narrow spaces. The biggest problem for rotary UAVs is the insufficient payload capacity required to carry heavy sensors, batteries, or other devices. Increasing the total thrust by increasing the number of rotors is a simple way to improve the payload capacity. Therefore, an overlapping octocopter with a compact structure and higher payload capacity is proposed in this study. Considering that wind gusts also affect outdoor aerodynamic performance, resulting in thrust or power variation, it is also important to investigate the hovering efficiency of the overlapping octocopter under crosswind conditions [7,8].

Tong et al. proposed an environmentally adaptive trajectory planning system to study the dynamic characteristics of UAVs under the effect of wind [9]. Sisson William et al. proposed a methodology to solve the issues with maneuver control [10]. Both studies are only limited to control theories. Recently, numerical simulations by Park H.S et al.

were applied on a rotorcraft fuselage using OpenFOAM software [11]. Jung Useok et al. tried a robust adaptive trajectory tracking control design for a rotorcraft subject to wind uncertainties [12]. As for the experiments, Bauknecht Andre et al. investigated the effect of operating parameters on aerodynamic performance based on a test bench with flow-field measurements [13]. It can be seen that there are few studies that are focused on the aerodynamic performance of rotary UAVs using both simulations and experiments. However, since wind gusts are normal during the flight of rotary UAVs, the blade element momentum (BEM) theory is presented as a reliable tool to analyze the performance of a UAV's rotor blade, and it is, therefore, possible to study the performance of its rotor in a wind gust. In particular, it is a challenge to maintain balance in horizontal wind as both the inflow and outflow are changed in this case [14,15].

Furthermore, a typical flying environment for UAVs normally includes a light breeze (1.6–3.3 m/s) or a gentle breeze (3.4–5.4 m/s). For an overlapping octocopter under the effect of horizontal wind, this paper is focused on answering the following questions: (1) How does a change in wind speed affect propulsive efficiency compared to a traditional octocopter? (2) Where does the higher thrust come from considering the stronger rotor interference and wind disturbance? Section 2 discusses the effect of horizontal wind on the rotor using blade element momentum theory. Section 3 presents numerical simulations to analyze the flow field of the overlapping octocopter with horizontal wind. Section 4 shows the wind tunnel tests and the experimental results. Finally, the conclusions are presented in Section 5.

2. Analysis of the Theoretical Model

The overlapping octocopter is presented in Figure 1, where the eight rotors are equally distributed and divided into two layers. Four rotors are located on each layer with an angle of 45° between the adjacent rotor arm, where Ω is the rotational speed of the rotor, T is the thrust generated by the rotor, and s is the length of the rotor arm. The optimal rotor spacing L = 1.8 D is proved with the best loading capacity [16], where L is the rotor spacing on the same layer, and D is the rotor diameter.

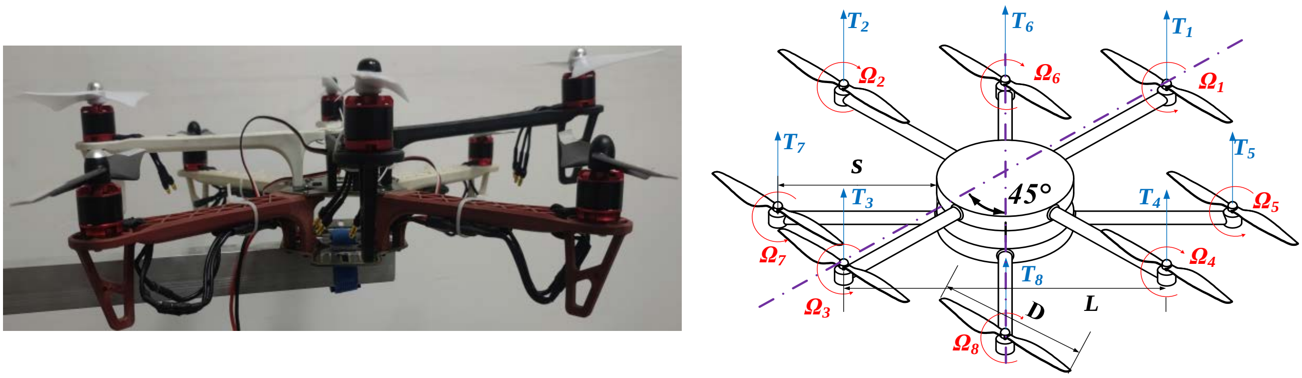

(**a**) (**b**)

Figure 1. Structure of the overlapping octocopter. (**a**) Prototype; (**b**) parameters.

2.1. Model Dynamics

The adjacent rotors on the same layer rotate in the opposite sense. Two sets of rotor motors on the diagonal turn in the same direction, providing the required thrust and torque for the vehicle, as shown in Figure 1b. Changing the thrust via the rotor speed allows for the transitional and rotational movement of the octocopter. In order to obtain a mathematical model of the octocopter, it is necessary to establish two coordinate systems, the inertial frame fixed on the earth $E = [x, y, z]^T$ and the body frame fixed attached to the vehicle $B = [X, Y, Z]^T$. The motion of an octocopter is described by six parameters ($x, y, z, \varphi, \theta, \psi$), where (x, y, z) is the position of the octocopter and (φ, θ, ψ) are the Euler angles, as shown in Figure 2 [17,18].

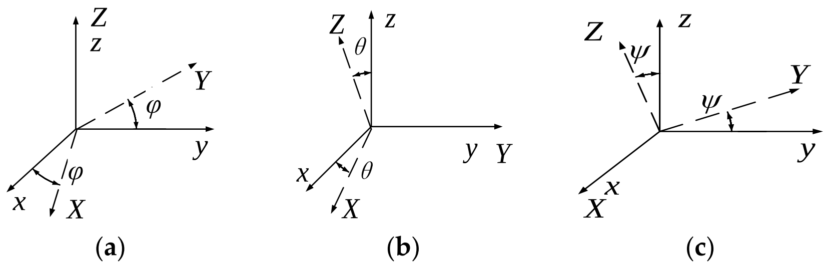

Figure 2. Euler angles. (**a**) Roll angle; (**b**) pitch angle; (**c**) yaw angle.

The rotation matrices on the X, Y and Z axes are as follows:

$$R(\varphi) = \begin{pmatrix} 1 & 0 & 0 \\ 0 & cos\ \varphi & -sin\ \varphi \\ 0 & sin\ \varphi & cos\ \varphi \end{pmatrix} \tag{1}$$

$$R(\theta) = \begin{pmatrix} \cos\theta & 0 & \sin\theta \\ 0 & 1 & 0 \\ -\sin\theta & 0 & \cos\theta \end{pmatrix} \tag{2}$$

$$R(\psi) = \begin{pmatrix} cos\ \psi & -sin\ \psi & 0 \\ sin\ \psi & cos\ \psi & 0 \\ 0 & 0 & 1 \end{pmatrix} \tag{3}$$

Finally, the conversion matrix R_{BE} and R_{EB} can be obtained as follows:

$$R_{BE} = \begin{bmatrix} cos\ \psi cos\ \theta & cos\ \psi sin\ \theta sin\ \varphi - cos\ \varphi sin\ \psi & cos\ \psi sin\ \theta cos\ \varphi + sin\ \psi sin\ \varphi \\ sin\ \psi cos\ \theta & sin\ \psi sin\ \theta sin\ \varphi + cos\ \varphi cos\ \psi & sin\ \psi sin\ \theta cos\ \varphi - sin\ \varphi cos\ \psi \\ -sin\ \theta & sin\ \varphi cos\ \theta & cos\ \theta cos\ \varphi \end{bmatrix} \tag{4}$$

$$R_{EB} = \begin{bmatrix} cos\ \psi cos\ \theta & sin\ \psi cos\ \theta & -sin\ \theta \\ cos\ \psi sin\ \theta sin\ \varphi - cos\ \varphi sin\ \psi & sin\ \psi sin\ \theta sin\ \varphi + cos\ \varphi cos\ \psi & sin\ \varphi cos\ \theta \\ cos\ \psi sin\ \theta cos\ \varphi + sin\ \psi sin\ \varphi & cos\ \psi sin\ \theta sin\ \varphi - cos\ \varphi sin\ \psi & cos\ \theta cos\ \varphi \end{bmatrix} \tag{5}$$

From Newton's second law, the linear motion of a UAV follows:

$$m\begin{pmatrix} \ddot{x} \\ \ddot{y} \\ \ddot{z} \end{pmatrix} = \begin{pmatrix} cos\ \varphi cos\ \theta sin\ \psi + sin\ \varphi sin\ \psi \\ cos\ \varphi sin\ \psi sin\ \theta - sin\ \varphi cos\ \psi \\ cos\ \varphi cos\ \theta \end{pmatrix} \sum_{i=1}^{8} F_i - m\begin{pmatrix} 0 \\ 0 \\ g \end{pmatrix} + F_{ext} \tag{6}$$

where F_i is the force of the i-th motor. F_{ext} is the external force caused by the horizontal wind. m is the vehicle mass and g is the gravity acceleration.

Then, the linear motion model of the vehicle can be expressed as:

$$\begin{cases} \ddot{x} = K_t \sum\limits_{i=1}^{8} [\Omega_i^2(cos\ \psi sin\ \theta cos\ \varphi + sin\ \psi sin\ \varphi) + F_{ext_x}]/m \\ \ddot{y} = K_t \sum\limits_{i=1}^{8} [\Omega_i^2(sin\ \psi sin\ \theta cos\ \varphi - sin\ \varphi cos\ \psi) + F_{ext_y}]/m \\ \ddot{z} = K_t \sum\limits_{i=1}^{8} [\Omega_i^2(cos\ \theta cos\ \varphi) + F_{ext_z}]/m - g \end{cases} \tag{7}$$

where K_t is the lift coefficient of the vehicle and $Kt = F_i/\Omega_i^2$.

An overlapping octocopter has not only linear motion but also angular motion. From the angular momentum theorem, we can obtain:

$$\vec{M} = \frac{d\vec{H}}{dt} \tag{8}$$

where $\vec{M}$ is the main moment of external forces applied to the vehicle, $\vec{H}$ is the angular momentum, and dt is the time deviation. When the angular velocity is $[p, q, r]^{\mathrm{T}}$, the above equation can be expressed as:

$$\vec{M} = \left.\frac{d\vec{H}}{dt}\right|_B + \begin{bmatrix} p \\ q \\ r \end{bmatrix} \times \vec{H} \tag{9}$$

where $\vec{H}$ is:

$$\vec{H} = \begin{pmatrix} I_x p - I_{xy} q - I_{xz} r + I_x \dot{M}_{ext_x} \\ -I_{yx} p + I_y q - I_{yz} r + I_y \dot{M}_{ext_y} \\ -I_{zx} p - I_{zy} q + I_z r + I_z \dot{M}_{ext_z} \end{pmatrix} \tag{10}$$

I is the moment of inertia and $I_{xy} = I_{yx} = I_{xz} = I_{zx} = I_{yz} = I_{zy} = 0$, M_{ext} is the external moment caused by the horizontal wind.

Substituting into Equation (9) gives:

$$\begin{pmatrix} M_x \\ M_y \\ M_z \end{pmatrix} = \begin{pmatrix} \mathrm{I}_x \dot{p} + I_x \ddot{M}_{ext_x} + (I_z - I_y) qr \\ \mathrm{I}_y \dot{q} + I_y \ddot{M}_{ext_y} + (I_x - I_z) pr \\ \mathrm{I}_z \dot{r} + I_z \ddot{M}_{ext_z} + (I_y - I_x) qp \end{pmatrix} \tag{11}$$

Then:

$$\begin{pmatrix} \dot{p} \\ \dot{q} \\ \dot{r} \end{pmatrix} = \begin{pmatrix} \left[M_x - I_x \ddot{M}_{ext_x} - (I_z - I_y) qr\right] I_x^{-1} \\ \left[M_y - I_y \ddot{M}_{ext_y} - (I_x - I_z) pr\right] I_y^{-1} \\ \left[M_z - I_z \ddot{M}_{ext_z} - (I_y - I_x) qp\right] I_z^{-1} \end{pmatrix} \tag{12}$$

The relationship between Euler's angle and angular velocity is as follows:

$$\begin{bmatrix} \dot{\varphi} \\ \dot{\theta} \\ \dot{\psi} \end{bmatrix} = \begin{bmatrix} 1 & tan\ \theta sin\ \varphi & tan\ \theta cos\ \varphi \\ 0 & cos\ \varphi & -sin\ \varphi \\ 0 & sin\ \varphi / cos\ \theta & cos\ \varphi / cos\ \theta \end{bmatrix} \begin{bmatrix} p \\ q \\ r \end{bmatrix} \tag{13}$$

Then, the angular motion model of the vehicle can be expressed as:

$$\begin{cases} \dot{p} = \left[s(T_1 + T_5 - T_3 - T_7) + (I_y - I_z) qr\right] / I_x + \ddot{M}_{ext_x} \\ \dot{q} = \left[s(T_4 + T_8 - T_2 - T_6) + (I_z - I_x) pr\right] / I_y + \ddot{M}_{ext_y} \\ \dot{r} = \left[s\left(\Omega_1^2 + \Omega_2^2 \cdots + \Omega_8^2\right) + (I_x - I_y) pq\right] / I_z + \ddot{M}_{ext_z} \end{cases} \tag{14}$$

2.2. Aerodynamic Model

Considering that the overlapping octocopter is more compact with two layers, the aerodynamic interference between the rotors becomes much more complicated compared to a traditional octocopter with equally distributed rotors or coaxial rotors, not to mention the wind effect. Figure 3 shows a model of rotor interference with no wind and rotor interference with the wind effect.

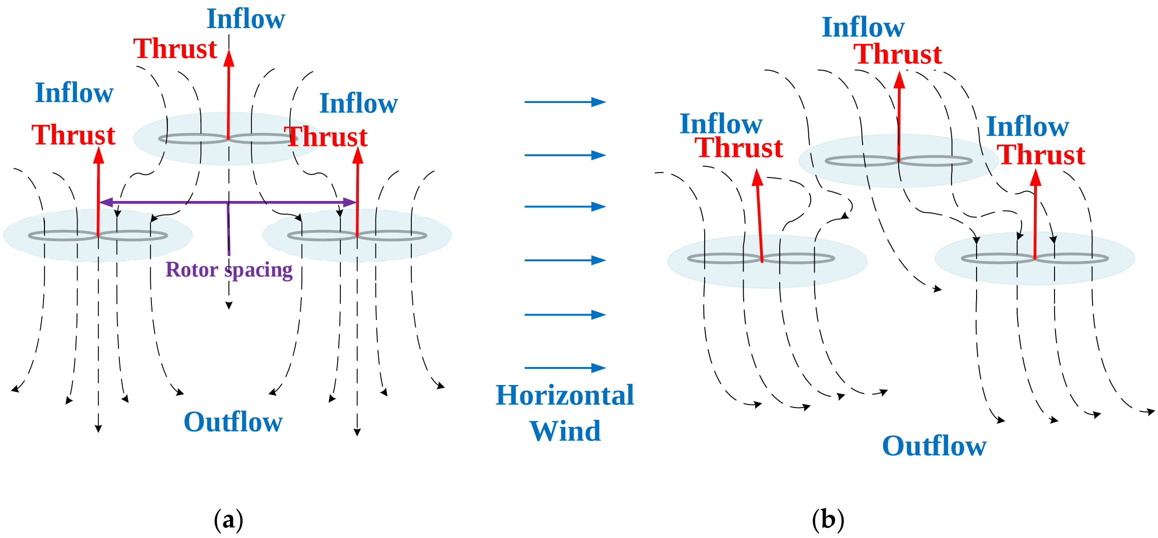

Figure 3. Rotor interference. (**a**) No wind; (**b**) with horizontal wind.

The rotor interference of the overlapping octocopter without the wind effect is focused on the upper rotors and lower rotors, where the air flow around the upper rotor may accelerate the inflow of the lower rotor and then cause extra power consumption or thrust with increased downwash flow of the lower rotor. When the horizontal wind is introduced, the airflow accelerated by the upper rotor is not evenly distributed between the lower rotors but deflected to one side along the wind direction. The downwash flow from the lower rotor is also tilted with a stronger rotor interference.

For a rotorcraft, momentum theory assumes that the rotor is an actuator disk embedded in a streamtube [19]. However, the streamtube may deform in the horizontal wind where the rotor inflow is not uniform with the wind effect. The net velocity of the rotor disk with the horizontal flow is contributed by both the incoming flow velocity and the rotor suction [15]. Figure 4 shows the rotor module with the wind effect in the streamtube.

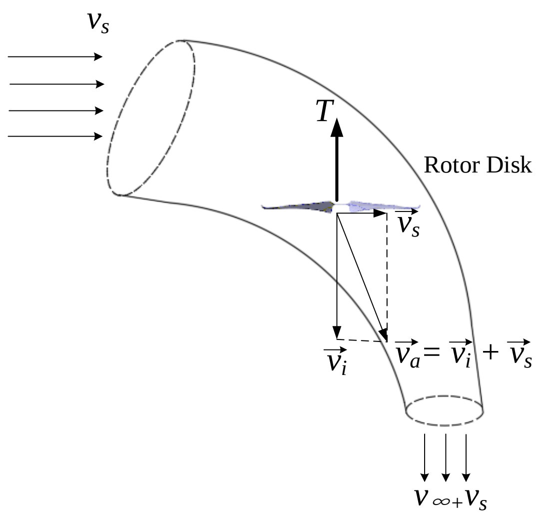

Figure 4. The rotor module with the wind effect in the streamtube.

The actual air velocity $\vec{v_a}$ with the acceleration by the rotor is the sum of the induced velocity $\vec{v_i}$ and the air flow rate $\vec{v_s}$. With the assumption of an incompressible fluid in the streamtube, the relationship between aerodynamic power P and thrust T is obtained [19].

$$T = 2\rho A v_i |v_a| \tag{15}$$

$$P = 2\kappa\rho A v_i^2 |v_a| \tag{16}$$

where A is the area of the rotor disk and ρ is the air density. $\kappa \geq 1$ is the induced power factor [20].

The horizontal incidence ratio μ and the vertical inflow ratio λ are defined as:

$$\lambda = \frac{2v_i}{\Omega D}; \mu = \frac{2v_s}{\Omega D} \tag{17}$$

Thus, the thrust and power of the rotor can be obtained as:

$$\mathrm{T} = \frac{1}{2}\rho A \Omega^2 D^2 \lambda \sqrt{\mu^2 + \lambda^2} \tag{18}$$

$$P = \kappa \frac{1}{2}\rho A \Omega^2 D^2 \lambda^2 \sqrt{\mu^2 + \lambda^2} \tag{19}$$

A simple relationship between rotor thrust and downwash flow can be easily obtained in the streamtube using the two physical laws of conservation of mass and conservation of momentum. Taking into account the geometry of the rotor blade, the expression for thrust given the inflow distribution across the rotor disk is derived by introducing the blade element theory on the basis of the momentum theory (Figure 5) [21]. A blade element is one small portion of the blade distance with r, from the center of rotation with a spanwise dimension,Δr. The thrust increment is given by:

$$\Delta T = b\frac{\rho}{2}\left(\Omega R + v_i\right)^2 a(\theta - \lambda) c \Delta r \tag{20}$$

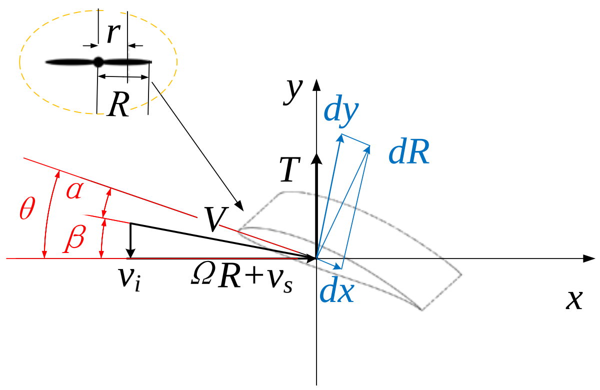

Figure 5. Aerofoil section of a blade at $r \in [0, R]$ from the rotor hub.

Mathematically, the thrust of the rotor is described by [22]:

$$\Delta T = b\int_0^R \frac{T}{\Delta r} dr = b\int_0^R \frac{\rho}{2}\left(\Omega R + v_i\right)^2 a\left(\theta - \frac{v_i}{\Omega R}\right) c dr \tag{21}$$

where b is the number of blades, R is the rotor radius, a is the slope of the lift curve, θ is the pitch angle of the blade element, and c is the chord of the blade element.

Compared with traditional octocopters with the same rotor size, including the planar octocopter with equally distributed rotors and the coaxial octocopter with four coaxial rotor pairs, the power coefficient and thrust coefficient is introduced:

$$C_T = \frac{4T}{\rho A (\Omega D)^2} \tag{22}$$

$$C_P = \frac{8P}{\rho A(\Omega D)^3} \tag{23}$$

Also, the figure of merit (FM) is presented to characterize the hovering performance [21].

$$\text{FM} = \frac{C_T^{3/2}}{\sqrt{2}C_P} = \frac{T^{3/2}}{P\sqrt{2\rho A}} \tag{24}$$

3. Simulations

3.1. Geometry

The rotor diameter is D = 400 mm, the height of the two rotor layers is h = 50 mm, and the rotor speed is 2200 rpm. Table 1 gives the basic parameters of the rotor blades used in the octocopter, and Figure 6 shows the chord length distribution.

Table 1. Rotor parameters.

Parameter	Value
Diameter	400 mm
Weight	0.015 kg
Number of blades	2
Chord length (75% R)	0.026 m
Rotor solidity	0.128

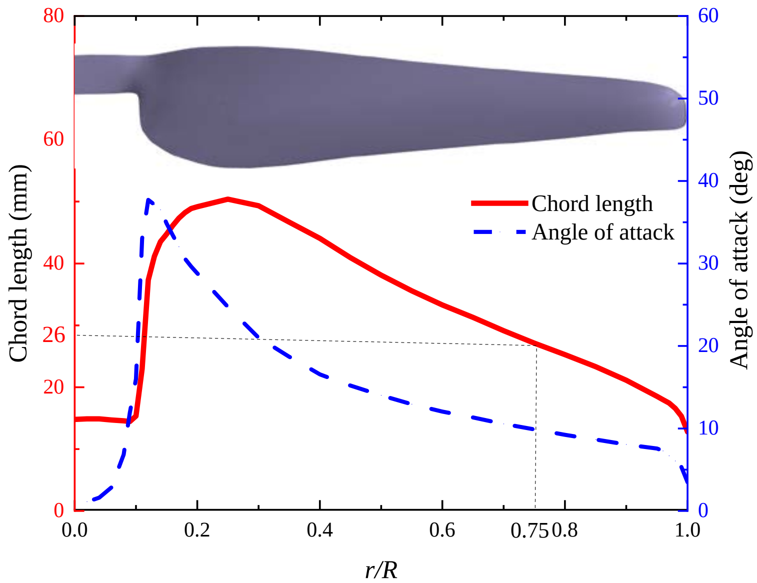

Figure 6. Aerofoil section of a blade at a radial station r ∈ [0, R] from the rotor hub.

3.2. Mesh Domain

Numerical simulations were performed by ANSYS (2021 R1) FLUENT. The size of the mesh domain was 18R (length) × 15R (width) × 15R (height) with a longer dimension (18R) to capture the flow detail along with the horizontal wind without extending computing time resulting from the excessive domain size. Table 2 is a domain independence check, which indicates that a smaller flow field led to excessive deviations in C_T, and when the size of the flow field reached 18R × 15R × 15R, it had almost no effect on C_T (0.029%). Also, a larger domain led to an increasing grid number with a longer computing time. The whole flow field was divided into eight rotational domains and one static domain, as shown in Figure 7.

Table 2. Domain independence.

Name	Mesh 1	Mesh 2	Mesh 3	Mesh 4	Mesh 5
Domain size	$12R \times 8R \times 8R$	$14R \times 10R \times 10R$	$16R \times 12R \times 12R$	$18R \times 15R \times 15R$	$22R \times 18R \times 18R$
C_T (2200 rpm)	0.175136	0.195458	0.203184	0.204452	0.204512
Relative error of C_T	10.397%	3.802%	0.620%	-	0.029%

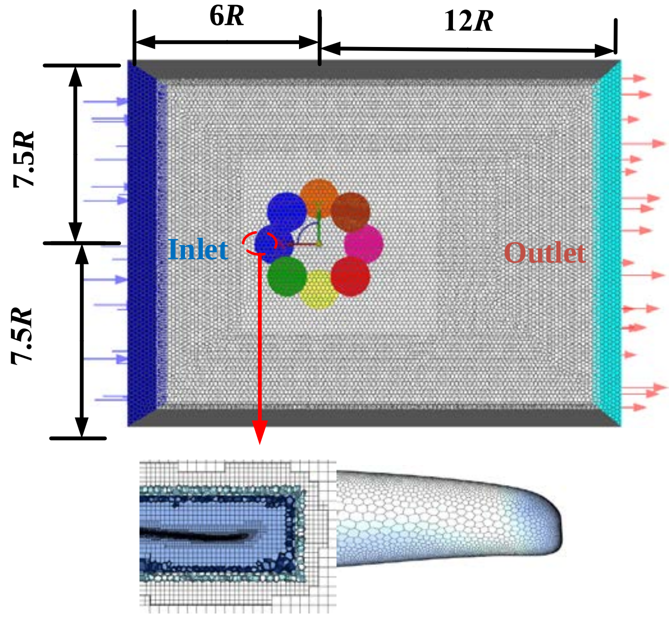

Figure 7. Computational grid for the overlapping octocopter.

The sliding-mesh method was applied to treat the boundaries between two domains. It did not involve the deformation and regeneration of the grid, so it did not cause a negative volume and also greatly saved the computational cost. The grids on the rotor tip were refined to reach the independence state by (1) running the initial simulation on the initial mesh and ensure the convergence of residual error to 10^{-5}, the monitor points were steady, and imbalances were below 1%. (2) Once it met the convergence criteria above for our first simulation, we refined the mesh globally in the domain. Generally, one should aim for around 1.5 times the initial mesh size. We ran the simulation and ensured that the residual error dropped below 10^{-5}, the monitor points were steady, and the imbalances were below 1%. Then, we compared the monitor point values with the values from the initial simulation to ensure they were the same or within the allowable tolerance. In this case, the solution was independent of the mesh [23,24]. The grid convergence is shown in Table 3.

Table 3. Tests of grid convergence.

Grid Normalized	Grid Spacing	C_T (2200 rpm)
1	1	0.204452
2	2	0.20245
3	4	0.195576

The order of convergence p observed from these results is

$$p = \ln\left(\frac{C_{T1} - C_{T2}}{C_{T1} - C_{T3}}\right) / \ln(2) = 1.779708 \tag{25}$$

For the theoretical convergence, the order is 2.0. Now, the Richardson extrapolation can be applied to obtain an estimate of C_T at zero grid spacing using the two finest grids.

$$C_{T\mathrm{h}=0} = C_{T1} + (C_{T1} - C_{T2})/(2^p - 1) \\ = 0.205275 \tag{26}$$

This value is also presented in Figure 8.

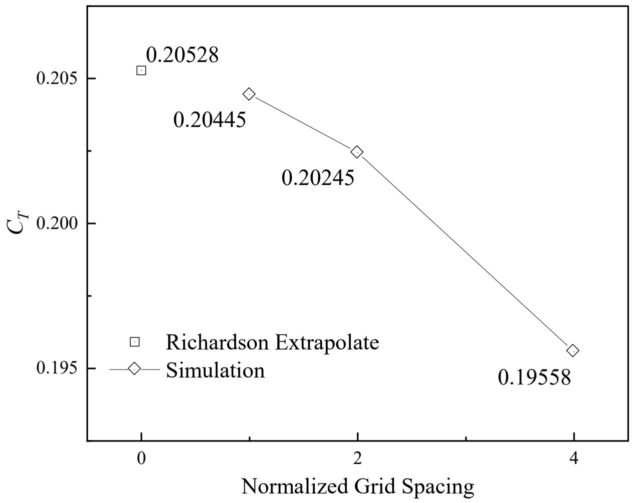

Figure 8. Richardson extrapolation.

We calculated the grid convergence index. Since three grids were used for the C_T calculations, a factor of safety FS = 1.25 was used. The GCI (grid convergence index) for grids 1 and 2 is:

$$\mathrm{GCl}_{12} = 1.25|(C_{T1} - C_{T2})/C_{T1}|/(2^p - 1)100\% = \\ 0.50297\% \tag{27}$$

The GCI for grids 2 and 3 is:

$$\mathrm{GCl}_{23} = 1.25|(C_{T2} - C_{T3})/C_{T2}|/(2^p - 1)100\% = \\ 1.0744\% \tag{28}$$

We checked if the solution was within the asymptotic convergence range

$$\mathrm{GCl}_{12}/(2^p\mathrm{GCl}_{23}) = 1.0098 \tag{29}$$

This value is approximately 1, indicating that the solution was well within the asymptotic convergence range. Thus, it can be considered that the thrust coefficient of the rotor was 0.205275 with an error range of 0.502%.

Finally, Mesh 4 was applied in the simulations. Additionally, a 20-layer boundary layer was applied around the rotor tips, and the grid properties are shown in Table 4. The initial y+ value in the first cells was between 1 and 30, and the final y+ was less than 1. For the low-Reynolds environment ($\mathrm{Re}_{\mathrm{tip}} < 10^5$), the effect of the y+ value was not very significant for the simulations, which is acceptable [24].

Table 4. Grid properties.

Initial y +	First Layer Height	Inflation Layer	Maximum Skewness	Minimum Orthogonal Quality	Elements
1	7.8×10^{-6}	20	0.8026	0.051	28,514,963
5	3.9×10^{-5}	16	0.8169	0.095	22,684,962
8	6.3×10^{-5}	14	0.8258	0.103	18,269,659
12	9.4×10^{-5}	10	0.8436	0.128	9,568,975
30	2.3×10^{-4}	8	0.8525	0.149	7,892,231

The Reynolds-averaged SST *k*–*ω* to deal with incompressible flows was used as the turbulence model. The semi-implicit method for pressure-linked equations (SIMPLE) was adopted for all simulations. Also, the PRESTO discretization gave more accurate results than the standard one since interpolation errors and pressure gradient assumptions on the boundaries are avoided. Furthermore, the second-order discretization schemes were utilized for the time discretization and convection and diffusion terms. Hence, this scheme prevents any unnecessary fluctuations in the solution fields. Lastly, the calculation convergence was considered when the residual errors were reduced to 10^{-5} to obtain the final results. In comparison, the traditional planar octocopter with equally distributed rotors and the coaxial octocopter were also simulated with the same procedure.

3.3. Results

Figure 9 shows the velocity distribution at the plane located on 1*D* beneath the overlapping octocopter.

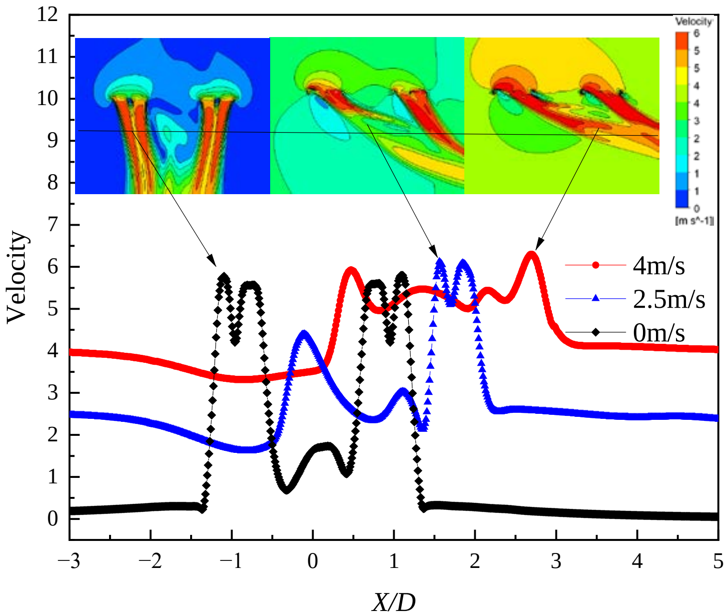

Figure 9. Velocity distribution of the downwash flow for the overlapping octocopter.

The velocity of the downwash flow accelerated with the increasing wind speed. Specifically, the maximum downwash flow was located at *X*/*D* = 1.1 and *X*/*D* = −1.1 without the wind effect and was symmetrically distributed. When the horizontal wind was introduced, the maximum downwash flow was at *X*/*D* = 1.5 for 2.5 m/s and *X*/*D* = 2.6 for 4 m/s, respectively.

Figure 10 shows the downwash flow distribution at 1*D* below the octocopter with a horizontal wind speed of 2.5 m/s. It is noted that the downwash flow of the coaxial octocopter was nearly not affected by the horizontal wind with a symmetrical structure, while the planar octocopter obtained a scatter distribution with the wind effect.

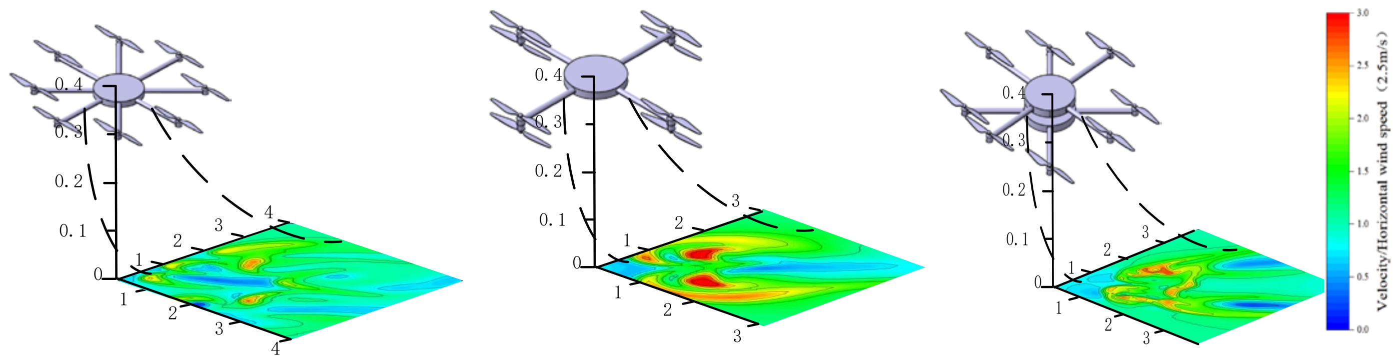

(**a**) (**b**) (**c**)

Figure 10. The downwash flow distribution at 1*D* below the octocopter with a horizontal wind of 2.5 m/s. (**a**) Planar octocopter; (**b**) coaxial octocopter; (**c**) overlapping octocopter.

Figure 11 shows the 3D vortex with the *Q*-criterion structure of the overlapping octocopter. As shown in Figure 11a, the rotor interference is mainly between the upper rotors and lower rotors with no horizontal wind, and the downwash flow is untapped with a symmetric distribution. The vortex began to move along with the wind and the vortices of the rotor appeared to deform and tangle with each other. Also, the wing tip vortices of the rotor were broken and reformed with the increasing wind speed. Finally, the interferences between the rotor and vortex and the vortex and vortex may decrease the aerodynamic performance by increasing power consumption [25].

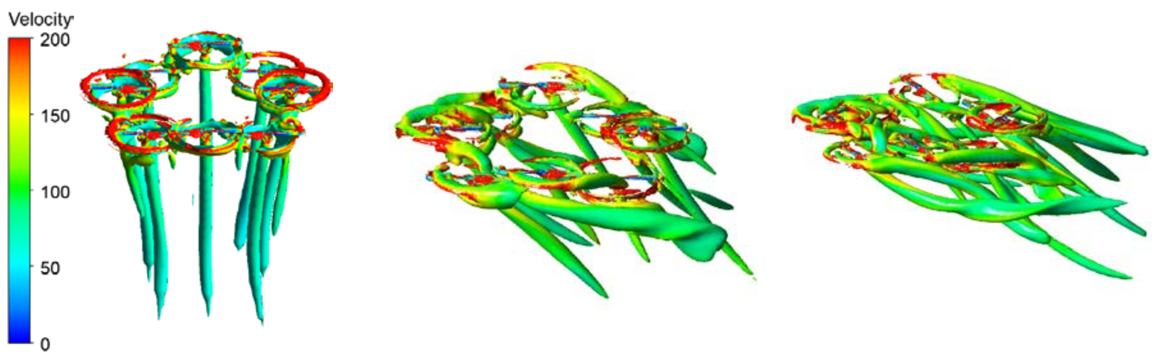

(**a**) (**b**) (**c**)

Figure 11. The vortex structure of the overlapping octocopter. (**a**) 0 m/s; (**b**) 2.5 m/s; (**c**) 4 m/s.

The pressure distribution of the overlapping octocopter in the horizontal wind is shown in Figure 12. The pressure difference on the upper and the lower surface increases gradually with the horizontal wind speed, which is directly related to the increment in the rotor thrust. Combined with the pressure on the rotor section as shown in Figure 12b–d, the pressure difference on the upper and lower surface of the rotor tip is significantly increased with the wind speed, which also leads to increased thrust with a better hover efficiency.

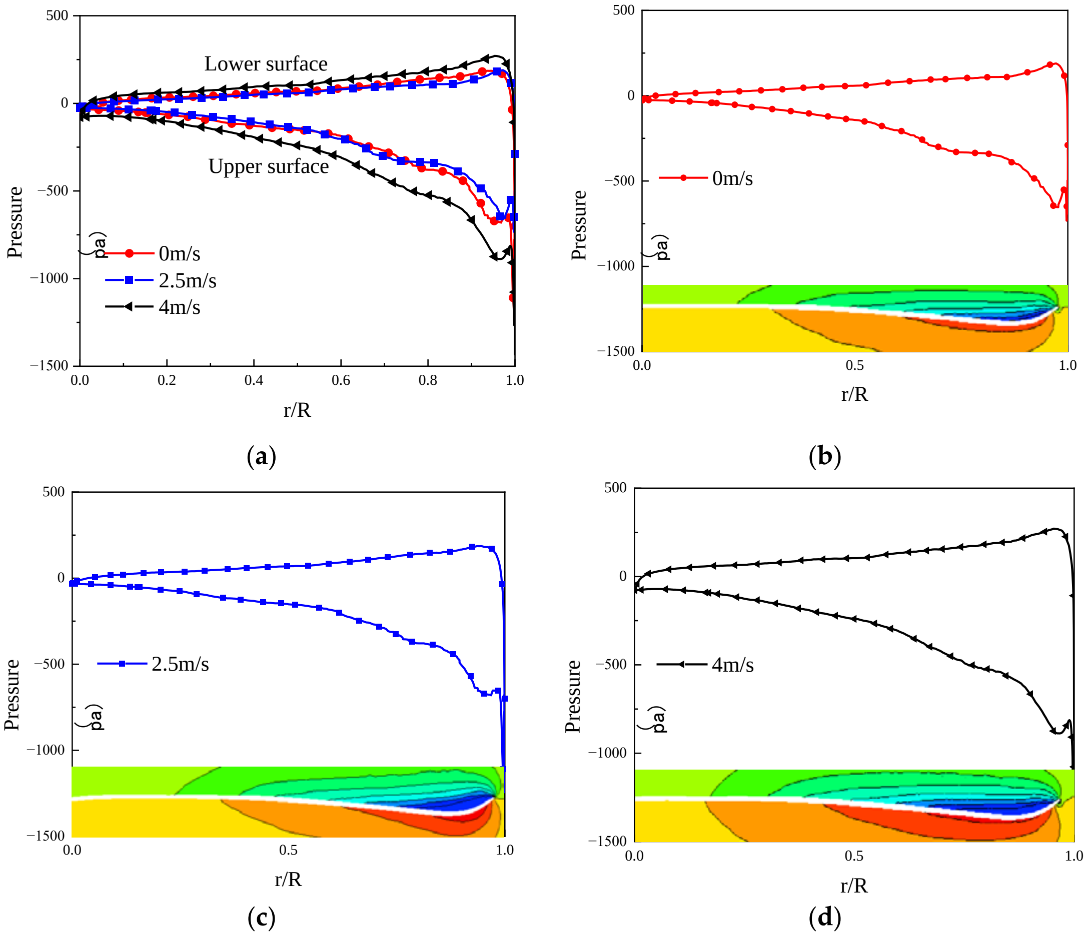

Figure 12. Pressure distribution. (**a**) Pressure comparison: (**b**) 0 m/s; (**c**) 2.5 m/s; (**d**) 4 m/s.

4. Wind Tunnel Tests

4.1. Facility and Experimental Setup

For this section, wind tunnel tests were conducted on the overlapping octocopter, planar octocopter, and coaxial octocopter as a comparison to investigate the wind effect on the octocopter with the same procedure. The experimental setup is shown in Figure 13. The test section of the low-speed wind tunnel was 3 m long × 3 m wide × 2.5 m high to guarantee sufficient maneuvering space. The wind was generated by two fans with a diameter of 3 m and a power of 45 kw, with a maximum wind speed of 50 m/s in the test section. The uncertainty of the wind speed was 0.4%. The octocopter was installed at a height of 1.5 m from the bottom to reduce the impact of the ground effect on the experiment. The rotor was powered by a BLDC motor (MSYS-LRK195.03). In the test, thrust was obtained with a thrust sensor (model: CZL605, accuracy: 0.02% f.s.), and power was obtained by collecting the voltage and the current (model: ABF-SS-L303SPV; accuracy: ±0.1 mV, ±0.1 µA). An optical tachometer was used to obtain the rotor RPM (model: DT-2234C, accuracy: ±0.05% + 1d) [16]. Table 5 shows the specific parameters and accuracy of the experiments.

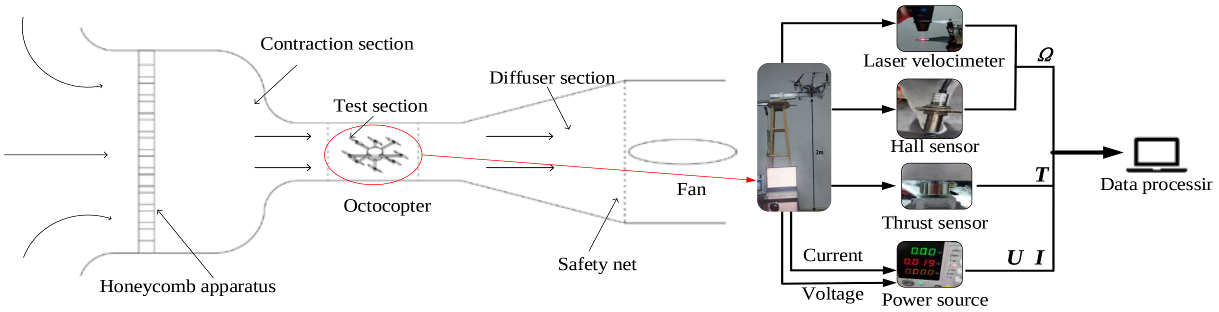

Figure 13. Experimental setup.

Table 5. Experimental parameters.

Parameter	Value
Density (kg/m^3)	1.185
Pressure (Pa)	1.01×10^5
Temperature (°C)	25
RPM	1500~2300
Wind speed (m/s)	0, 2.5, 4 (±0.4%)

4.2. Results

Figure 14 compares the thrust coefficient obtained from numerical simulations and the experiments. Both the simulations and experiments are generally in good agreement with an acceptable relative error of 2% [26], especially for a higher rotor speed, where a stronger rotor interference may cause rotor vibration with a variation in the thrust measurement. Additionally, the error mainly came from (1) the deformation of the rotor during the experiment when it was treated as a rigid body in the simulation and (2) the standard deviations of the rotational speed and the mean voltages from the thrust sensors in the experiments which are related to the finite number of magnets that excite the Hall effect sensor.

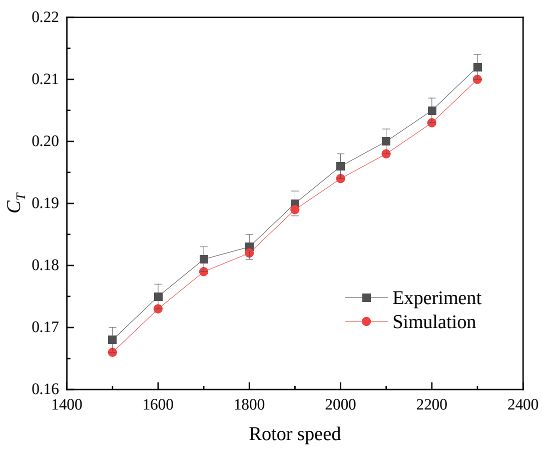

Figure 14. Comparison of simulations and experiments.

The variation in the thrust coefficient for the different octocopters at 2.5 m/s and 4 m/s is shown in Figure 15. As expected, the thrust is directly related to the pressure difference. A higher rotor speed also led to a greater pressure difference. In addition, the horizontal wind became advantageous to the thrust increment, especially at a higher wind speed. The maximum thrust variation reached was 6.89% in this case. For the coaxial octocopter, the thrust was lower than the other two octocopters. For the same wind speed, as shown in Figure 12, the pressure difference on the rotor surface allowed the rotor to generate higher thrust.

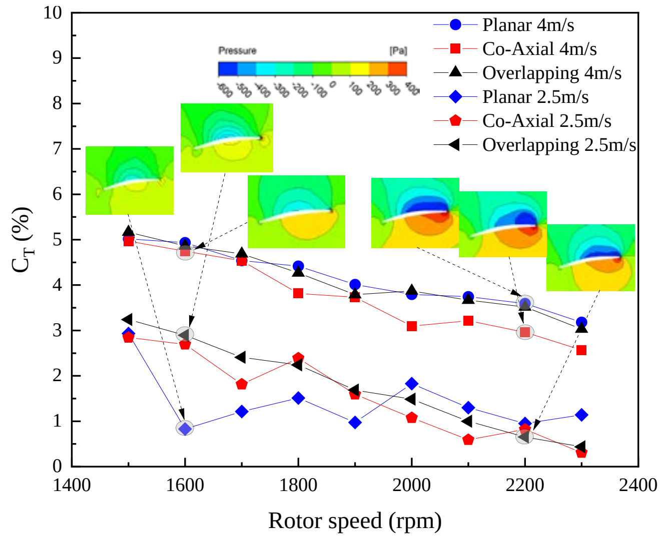

(**a**)

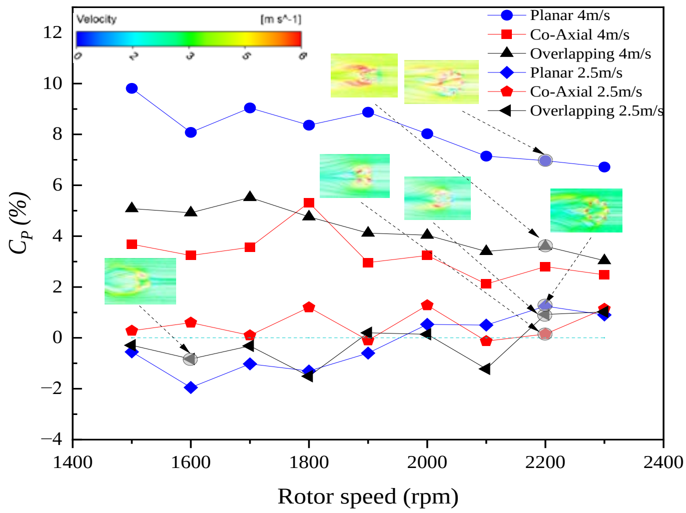

(**b**)

Figure 15. Thrust and power coefficient increment for different octocopters. (**a**) Thrust coefficient and pressure at rotor tip (75%); (**b**) power coefficient and streamline.

The power coefficient increased with the wind speed where the rotor interference was much stronger along with the wind, especially for the wind at 2.5 m/s with a lower rotor speed of less than 1900 rpm. Surprisingly, the power decreased with the rotor speed, with a maximum reduction of 1.5%, which means that increasing the rotor speed will offset the rotor interference to some extent. For the 4 m/s horizontal wind, there was a significant increase in the power coefficients at 1800 rpm for the planar octocopter, which decreased the hover efficiency of the vehicle. Together with the streamline, the flow field of the vehicle became even more chaotic at 4 m/s, especially for the planar octocopter. The maximum increment in the power coefficient was up to 9.81%. For the same horizontal wind speed, increasing the rotor speed may improve the hover efficiency of the octocopter.

The figure of merit (FM) of the overlapping octocopter with different wind speeds is shown in Figure 16.

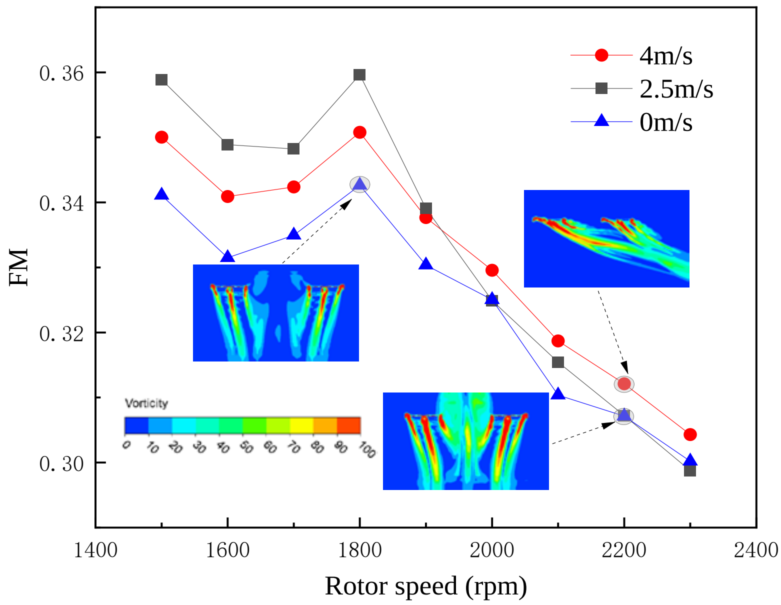

Figure 16. Figure of merit and the rotor vortices.

The FM of the overlapping octocopter tended to decrease with the increasing rotor speed. It can be seen that the vortex diffused and merged. This vortex generation has a negative effect on the FM of the rotor blades [27]. Compared with no wind effect, an increase in the FM of the overlapping octocopter was observed in the presence of horizontal wind. This is because the vortices generated by the rotor are blown away from the surface of the rotor due to the horizontal wind, thus reducing the interference between the vortices and the rotor. In particular, the FM of the overlapping octocopter increased significantly at the lower rotational speed of 2.5 m/s. The maximum value of FM was 0.36 at 1800 rpm, which led to the improved aerodynamic performance of the octocopter. However, as the wind speed increased, this advantage was not that obvious, with a slight decrement. This may have been caused by the increasing power consumption to maintain stability in the wind at 4 m/s.

Figure 17 shows the variation in the FM for the three octocopters in horizontal wind.

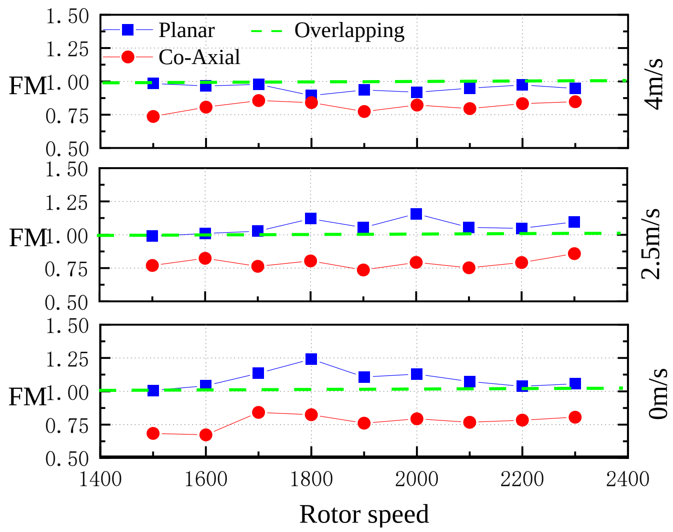

Figure 17. FM variation.

The FM of the coaxial octocopter reached the minimum level without a wind effect. The planar octocopter reached the maximum FM at 0 and 2.5 m/s with a rotor speed ranging from 1800 to 2000 rpm. However, it decreased with the increasing wind speed, which indicates that the planar octocopter was not suitable for flying at a higher wind speed. Interestingly, both the planar and coaxial octocopter presented a lower FM, while the overlapping octocopter obtained a higher FM with a better hover efficiency and the ability to resist wind gusts.

5. Conclusions

In this paper, the aerodynamic performance of an overlapping octocopter with the effect of horizontal wind was investigated using numerical simulations and experiments and compared to a traditional planar octocopter and coaxial octocopter. The conclusions are as follows:

(1) The overlapping octocopter obtained the highest FM with an increasing wind speed, which proves that the overlapping rotor arrangement is inclined to improve the hover efficiency with the horizontal wind effect, especially for a higher rotor speed. The simulation results indicated that the thrust increased with the pressure difference resulting from the wind effect. In this case, the overlapping octocopter is proven to have a better aerodynamic performance in the gentle breeze (3.4–5.4 m/s) and excellent potential for exploration in a crosswind with a compact structure.

(2) The coaxial octocopter showed decreased aerodynamic performance with or without a wind effect, which may have been caused by the stronger rotor interference between

the upper and lower rotor. On the contrary, the hover efficiency of the planar octocopter showed a similar tendency at 0m/s and 2.5 m/s, which may lead to wider applicability without a wind effect and with size limitations.

(3) For the overlapping octocopter, the horizontal wind had a positive effect, significantly increasing the pressure difference on the rotor surface, which in turn increased the thrust generated by the rotor. Compared with no horizontal wind, the thrust coefficient increased by 5.16% at 1500 rpm with a wind speed of 4 m/s. In this case, the horizontal wind increases the intensity of the downwash flow; the vortex movement is accelerated along with the wind, which offsets the power consumption and leads to a higher FM.

(4) For a lower rotor speed of less than 1800 rpm, the power consumption decreased with rotor interference and wind disturbance. It was reduced by 1.95% at 1600 rpm for 2.5 m/s compared with the planar octocopter without the wind effect. For the higher rotor speed of more than 2000 rpm, the thrust increased with the wind speed. This led to a maximum of 10% compared with the planar octocopter at 2000 rpm and at 4 m/s. Thus, for the octocopter, reducing the rotor speed in a light breeze or increasing the rotor speed in a gentle breeze will improve the hover efficiency.

Author Contributions: Y.L. (Yao Lei) carried out experiments; J.W. wrote the manuscript with the assistance of Y.L. (Yao Lei) and performed the new set of simulations. Y.L. (Yazhou Li) revised the manuscript. All authors have read and agreed to the published version of the manuscript.

Funding: This research was supported by the National Natural Science Foundation of China (Grant No. 52275095) and the Fujian Provincial Industrial Robot Basic Components Technology Research and Development Center (2014H2004).

Data Availability Statement: All data are already included in the manuscript.

Acknowledgments: The authors thank the Key Laboratory of Fluid Power and Intelligent Electro-Hydraulic Control (Fuzhou University), Fujian Province University, and Fuzhou University Jinjiang Science and Education Park for performing the experiments.

Conflicts of Interest: The authors declare no conflict of interest.

References

1. Nawaz, H.; Ali, H.M.; Massan, S. Applications of unmanned aerial vehicles: A review. *Tecnol. Glosas InnovaciÓN Apl. Pyme. Spec* **2019**, *2019*, 85–105. [CrossRef]
2. AL-Dosari, K.; Hunaiti, Z.; Balachandran, W. Systematic Review on Civilian Drones in Safety and Security Applications. *Drones* **2023**, *7*, 210. [CrossRef]
3. Liu, Z.; Li, J. Application of Unmanned Aerial Vehicles in Precision Agriculture. *Agriculture* **2023**, *13*, 1375. [CrossRef]
4. Jalayer, M.; O'Connell, M.; Zhou, H.; Szary, P.; Das, S. Application of Unmanned Aerial Vehicles to Inspect and Inventory Interchange Assets to Mitigate Wrong-Way Entries. *ITE J.* **2019**, *36*, 42.
5. Aboulafia, R. Military rotorcraft: Strongest aero market. *Aerosp. Am.* **2011**, *49*, 8.
6. Basset, P.M.; Vu, B.D.; Beaumier, P.; Reboul, G.; Ortun, B. Models and Methods at ONERA for the Presizing of eVTOL Hybrid Aircraft Including Analysis of Failure Scenarios. In Proceedings of the AHS International 74th Annual Forum & Technology Display, Phoenix, AZ, USA, 14–17 May 2018.
7. Wei, P.; Lin, X.; Kong, Z. System identification of wind effects on multirotor aircraft. *Int. J. Intell. Robot. Appl.* **2021**, *6*, 1. [CrossRef]
8. González-Rocha, J.; De Wekker, S.F.; Ross, S.D.; Woolsey, C.A. Wind Profiling in the Lower Atmosphere from Wind-Induced Perturbations to Multirotor UAS. *Sensors* **2020**, *20*, 1341. [CrossRef]
9. Tong, C.; Liu, Z.; Dang, Q.; Wang, J.; Cheng, Y. Online environmentally adaptive trajectory plan-ning for rotorcraft unmanned aerial vehicles. *Aircr. Eng. Aerosp. Technol.* **2023**, *95*, 2.
10. Sisson, W.; Karve, P.; Mahadevan, S. Digital twin for component health- and stress-aware rotorcraft flight control. *Struct. Multidiscip. Optim.* **2022**, *65*, 11. [CrossRef]
11. Park, H.S.; Linton, D.; Thornber, B. Rotorcraft fuselage and ship airwakes simulations using an immersed boundary method. *Int. J. Heat Fluid Flow* **2022**, *9*, 3. [CrossRef]
12. Jung, U.; Cho, M.G.; Woo, J.W.; Kim, C.J. Trajectory-Tracking Controller Design of Rotorcraft Using an Adaptive Incremental-Backstepping Approach. *Aerospace* **2021**, *8*, 248. [CrossRef]
13. Bauknecht, A.; Wang, X.; Faust, J.A.; Chopra, I. Wind Tunnel Test of a Rotorcraft with Lift Compounding. *J. Am. Helicopter Soc.* **2021**, *66*, 1. [CrossRef]

14. Lee, Y.B.; Park, J.S. Hover Performance Analyses of Coaxial Co-Rotating Rotors for eVTOL Aircraft. *Aerospace* **2022**, *9*, 152. [CrossRef]
15. Gill, R.; D'Andrea, R. Computationally Efficient Force and Moment Models for Propellers in UAV Forward Flight Applications. *Drones* **2019**, *3*, 77. [CrossRef]
16. Lei, Y.; Wang, H. Aerodynamic Optimization of a Micro Quadrotor Aircraft with Different Rotor Spacings in Hover. *Appl. Sci.* **2020**, *10*, 1272. [CrossRef]
17. Zou, A.M.; Fan, Z. Fixed-Time Attitude Tracking Control for Rigid Spacecraft Without Angular Velocity Measurements. *IEEE Trans. Ind. Electron.* **2020**, *67*, 99. [CrossRef]
18. Zhao, K.; Zhang, J.; Ma, D.; Xia, Y. Composite Disturbance Rejection Attitude Control for Quadrotor With Unknown Disturbance. *IEEE Trans. Ind. Electron.* **2019**, *67*, 6894–6903. [CrossRef]
19. Lee, S.; Dassonville, M. Iterative Blade Element Momentum Theory for Predicting Coaxial Rotor Performance in Hover. *J. Am. Helicopter Soc.* **2020**, *65*, 1–12. [CrossRef]
20. Moses, B.; Robert, M. Thrust Control for Multirotor Aerial Vehicles. *IEEE Trans. Robot.* **2017**, *33*, 2.
21. Garofano-Soldado, A.; Sanchez-Cuevas, P.J.; Heredia, G.; Ollero, A. Numerical-experimental evaluation and modelling of aerodynamic ground effect for small-scale tilted propellers at low Reynolds numbers. *Aerosp. Sci. Technol.* **2022**, *126*, 107625. [CrossRef]
22. Nishio, T.; Sunada, S.; Yamaguchi, K.; Tanabe, Y.; Yonezawa, K.; Tokutake, H. Note on a Method for Simulating Rotor Motion when Accelerating During Descent. *Trans. Jpn. Soc. Aeronaut. Space Sci. Aerosp. Technol. Jpn.* **2019**, *17*, 577–581. [CrossRef]
23. Yasuda, H.; Kitamura, K.; Nakamura, Y. Numerical Analysis of Flow Field and Aerodynamic Characteristics of a Quadrotor. *Trans. Jpn. Soc. Aeronaut. Space Sci. Aerosp. Technol. Jpn.* **2013**, *11*, 10. [CrossRef]
24. Lei, Y.; Wang, J.; Li, Y.; Gao, Q. In-Hover Aerodynamic Analysis of a Small Rotor with a Thin Circular-Arc Airfoil and a Convex Structure at Low Reynolds Number. *Micromachines* **2023**, *14*, 540. [CrossRef] [PubMed]
25. Park, H.S.; Kwon, J.O. Numerical Study about Aerodynamic Interaction for Coaxial Rotor Blades. *Int. J. Aeronaut. Space Sci.* **2020**, *22*, 2. [CrossRef]
26. Lakshminarayan, K.V.; Baeder, D.J. Computational Investigation of Microscale Coaxial-Rotor Aerodynamics in Hover. *J. Aircr.* **2010**, *47*, 3. [CrossRef]
27. Abraham, A.; Leweke, T. Experimental investigation of blade tip vortex behavior in the wake of asymmetric rotors. *Exp. Fluids* **2023**, *64*, 6. [CrossRef]